bioRxiv preprint doi: https://doi.org/10.1101/760835; this version posted September 8, 2019. The copyright holder for this preprint (which was not certified by peer review) is the author/funder, who has granted bioRxiv a license to display the preprint in perpetuity. It is made available under aCC-BY-NC-ND 4.0 International license.

Anatomic set of mechanical models for the organ of Corti

Jorge Berger[a,1,2] **and Jacob Rubinstein**[b,1]

[a]Department of Physics and Optical Engineering, Ort Braude College, Karmiel, Israel; [b]Department of Mathematics, Technion, Haifa, Israel

This manuscript was compiled on August 13, 2019

A new model for the mechanical and hydrodynamical processes in the organ of Corti (OoC) is proposed. In this model the motion of the basilar membrane is provided as input, and we concentrate on the other components of the OoC. The model consists of a set of equations, all based on Newton's laws, describing the motions and mutual interactions of the outer hair cells, the outer hair bundles, Deiter cells, the reticular lamina, Hensen cells, and the inner hair bundle. In addition, the model includes the equations describing the endolymph fluid motion in the subtectorial channel. Key ingredients in the model are the nonlinear constitutive laws governing the vibrations of the outer hair bundles and outer hair cells. The inner hair bundle oscillates via interaction with the endolymph flow. It is shown that under a minimal set of assumptions, and using basic mechanical principles, the components of the OoC listed above can act as a second filter, along with the basilar membrane filter, that enhances frequency selectivity, amplitude compression and signal to noise ratio.

cochlea | hair cell | second filter | critical oscillator

1.

Hearing in mammals involves a long chain of transductions (1–7). Pressure oscillations are collected from the air by the outer ear, and used by the middle ear to shake perilymph in the inner ear, while reducing the impedance mismatch. The wavelength of sound in perilymph is longer than the entire cochlea, but the partitioned structure of the cochlea extracts from it a traveling surface wave with shrinking wavelength, that deposits most of its energy at a short segment of the partition (8, 9). Most of the elastic energy delivered to the cochlear partition resides at the basilar membrane (BM).

We will focus on a layer of the organ of Corti (OoC), that senses the vibrations at a particular position in the BM, transmits them to the corresponding inner hair bundle (IHB), and from there to the auditory nerve. From the present point of view, motion of the BM will be the 'input,' and motion of the IHB, the 'output.' Accordingly, in this treatment the OoC does not include the BM. The shape of the OoC in the basal region of the cochlea is quite different than the shape near the apex; we will have in mind the OoC in the basal region, where higher frequencies are detected, and where the OoC has the greatest impact on amplification and frequency selectivity.

Figure 1 is a schematic drawing (not to scale) of the OoC, showing the components with which we will deal. It should be noted that whereas the outer hair bundles (OHBs) are attached to the tectorial membrane (TM), the IHB is not. As a consequence, when a cuticular plate [the top of an outer hair cell (OHC)] rises, the corresponding OHB tilts clockwise; on the other hand, motion of the reticular lamina (RL) has no direct effect on the inclination of the IHB. In order to turn the IHB and send a signal to the auditory nerve, endolymph flux in the subtectorial channel is required.

Substantial evidence has led to the conclusion that the OoC compresses the amplitudes and tunes the frequencies of the vibrations transferred from the stapes to the BM. By taking motion of the BM as the input, we will be investigating the more controversial question of whether there is an additional filter that provides further compression and tuning on the way from the BM to the auditory nerve (10–15). The conjecture of such a "second filter" is usually attributed to motion of the TM, but our analysis indicates that this feature is not necessary.

Our aspiration is not to obtain accurate values for the mechanical performance of the OoC, but rather to gain insight on how its components cooperate to achieve this performance. We would like to answer questions such as: Why the IHB is not attached to the TM? Or, why after transforming fluid flow into mechanical vibration, this vibration is transformed back into fluid flow, this time along a narrow channel, involving high dissipation. Is there any advantage of having several OHCs, rather than a single stronger OHC? How does an OHC perform mechanical work on the system? Is there any role to passive components such as the Hensen cells (HC)?

Many theoretical treatments fall into an extreme category. At one extreme, mechanical activity of the OoC is substituted by an equivalent circuit, and it's not clear where Newton's laws come in. At the other extreme, the OoC is divided into thousands of pieces, and a finite elements calculation is carried out (16–18). Neither of these approaches enables us to answer the questions above. Our approach involves postulating a simplified model for each component, with idealized geometry and with as few elements and forces as possible, hoping to capture the features that are essential for its functioning. After the models are chosen, Newton laws can be meticulously followed.

Significance Statement

The organ of Corti (OoC) transfers vibrations in the inner ear to the auditory nerve, while amplifying, filtering, and adapting them. In spite of decades of intense study, there is no full consensus on its mechanical activity. While most of the work on the OoC concentrates on the basilar membrane (BM), we consider the BM's vibration as given input, and provide a platform that enables testing the influence of possible models for each of its components on the performance of the OoC. The present set of models could explain the high frequency selectivity, amplitude compression, and signal/noise ratio of the OoC.

[1]Both authors contributed equally to this work.

[2]To whom correspondence should be addressed. E-mail: jorge.berger@braude.ac.il

DRAFT

bioRxiv preprint doi: https://doi.org/10.1101/760835; this version posted September 8, 2019. The copyright holder for this preprint (which was not certified by peer review) is the author/funder, who has granted bioRxiv a license to display the preprint in perpetuity. It is made available under aCC-BY-NC-ND 4.0 International license.

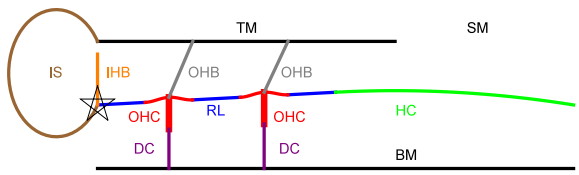

Fig. 1. Schematic drawing, showing the components of the OoC. TM: tectotial membrane; SM: scala media; IS: inner sulcus; IHB: inner hair bundle; OHB: outer hair bundle; OHC: outer hair cell; RL: reticular lamina (set of blue segments); HC: Hensen cells; DC: Deiter cell; BM: basilar membrane. The top of each OHC will be called 'cuticular plate' (CP). The model for each of these components is spelled out in Section 4. The star marks the position that is taken as the origin, $x = y = 0$.

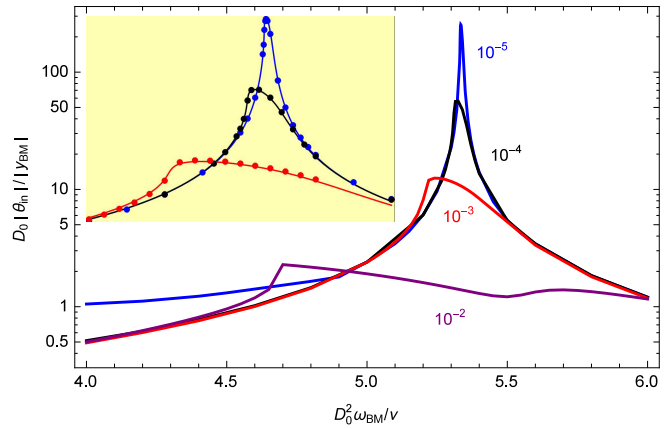

Fig. 2. Gain supplied by the OoC. $|\theta_{\rm in}|$ is the root mean square (rms) amplitude of the deflection angle of the IHB and $|y_{\rm BM}|$ is the rms amplitude of the height of the BM at the point where it touches the DC, $y_{\rm BM} = A\cos\omega_{\rm BM}t$ ($|y_{\rm BM}| = A/\sqrt{2}$). The value of A is marked next to each curve. In these evaluations we have ignored thermal noise. Inset: the dots are calculated values for our system and the lines follow Eq. [1] with the fitted values $|B| = 1.8\times10^3$, $\alpha = 6.6\times10^{-4}$, $\chi_1 = -0.66$ (for the three lines). Our units are specified in section 3B.

The most important difference between our models and those we have found in the literature is that pressure in the subtectorial channel is a function of position and time, that exerts large forces along the RL. Another salient difference is that the RL is not regarded as a completely rigid body, but rather the cuticular plates (CPs) can form mild bulges or dents in response to the local forces exerted by the corresponding OHC and OHB.

As supporting information we provide a mathematica code. This code is modular, so that not only the parameters can be varied, but also the models.

2. Main Results

We regard the maximal contraction of the OHC, Δ, as a control parameter, i.e., the parameter that quantifies the power generated within the system, and find that the OoC behaves as a critical oscillator (see *Supporting Information*): when the control parameter is larger than the bifurcation (critical) value Δ_c, the system undergoes spontaneous oscillations. For the parameters in Table 1, we found $\Delta_c = 0.254D_0$ and in the limit $\Delta \to \Delta_c$ the oscillation frequency is $\omega_c = 5.338$ in units of ν/D_0^2; D_0 is the "height" of the subtectorial channel and ν the kinematic viscosity of endolymph. In the following we assume that the OoC is adjusted to this bifurcation value, $\Delta = \Delta_c$.

We denote by $|\theta_{\rm in}|$ the amplitude of the output (inclination of the IHC) and by $|y_{\rm BM}|$ the amplitude of the input (deviation of the BM from its equilibrium position). Following the general behavior of critical oscillators near bifurcation (see *Supporting Information*), for $\Delta = \Delta_c$, input frequency $\omega \approx \omega_c$ and small $|y_{\rm BM}|$, the gain is given by

$$\frac{|\theta_{\rm in}|}{|y_{\rm BM}|} = \frac{1}{|B|\sqrt{\alpha^2(\omega-\omega_c)^2 + 2\alpha\cos\chi_1\,(\omega-\omega_c)|\theta_{\rm in}|^2 + |\theta_{\rm in}|^4}}\,, \qquad [1]$$

where B, α and χ_1 are constants.

Figure 2 shows the gain as a function of the frequency, for several amplitudes of $y_{\rm BM}$. Our results show remarkable similarity to those of the gain of the BM with respect to the stapes (19, 20), suggesting that the OoC performs two filtering operations: from the stapes to the BM (not studied here), and from the BM to the IHB. In both cases, weaker inputs acquire larger amplification and tighter selectivity. Except for the case of lowest amplitude, the gain becomes independent of the amplitude far from the resonance frequency.

The gain curves are skewed, providing a faster cut at lower frequencies than at higher frequencies. This feature is complementary to the selectivity provided by the cochlear partition, that provides a fast cutoff for high frequencies. Experimental support for faster cutoff of frequencies below the resonance can be found in the comparison of the pressure levels required to shake the BM with a given amplitude against those required to excite the auditory nerve (13, 15, 20). Note that since the gain depicted in Fig. 2 considers given amplitudes of $|y_{\rm BM}|$, the relevant lines for comparison with the auditory nerve tuning curves are the isodisplacements contours. Note also that the resonance for faint amplitudes can be missed in the measurements of the auditory nerve threshold: for instance, if the smallest audible amplitude is $A = 10^{-5}D_0$ at the best frequency, corresponding to an order of magnitude below the typical threshold amplitudes in Refs. (13) and (20), then it follows from the curves in Fig. 2 that if $\omega_{\rm BM}$ changes by just 0.6%, the amplitude required to yield the same excitation of the IHB would be $A = 10^{-4}D_0$ (i.e., 20 dB difference).

The inset in Fig. 2 is an expansion of the range $5.1 \le \omega_{\rm BM} \le 5.5$. It shows that the gains for moderate amplitudes behave as expected from a critical oscillator in the vicinity of the bifurcation point.

If the transduction from the BM to the IHB has critical oscillator behavior, then the amplitude compression at resonance of neural activity should be larger than that of BM motion. Indirect experimental support for this scenario is provided by measurements of the OoC potential (21) and of the ratio between the amplitudes of motion of the RL and the BM (22).

Figures 3 and 4 compare the time dependencies of the input and of the output in the case of a small signal when noise is present. The signal had the form $y_{\rm BM} = A\cos\omega_{\rm BM}t$ during the periods $2000 < t < 4000$ and $6000 < t < 8000$, and was off for $0 < t < 2000$ and $4000 < t < 6000$. We took $A = 3\times10^{-5}$ and $\omega_{\rm BM} = 5.329$ (which corresponds to the highest gain for this amplitude). Our model for noise is described in Section 4L. The input $y_{\rm total}(t)$ is the sum of the signal and the noise. Panel A in each of these figures shows the entire range $0 < t < 8000$, and the other panels focus on selected ranges.

Figure 3B shows $y_{\rm total}(t)$ in a range such that during the first half only noise is present, whereas during the second half also the signal is on. It is hard to notice that the presence of

DRAFT

bioRxiv preprint doi: https://doi.org/10.1101/760835; this version posted September 8, 2019. The copyright holder for this preprint (which was not certified by peer review) is the author/funder, who has granted bioRxiv a license to display the preprint in perpetuity. It is made available under aCC-BY-NC-ND 4.0 International license.

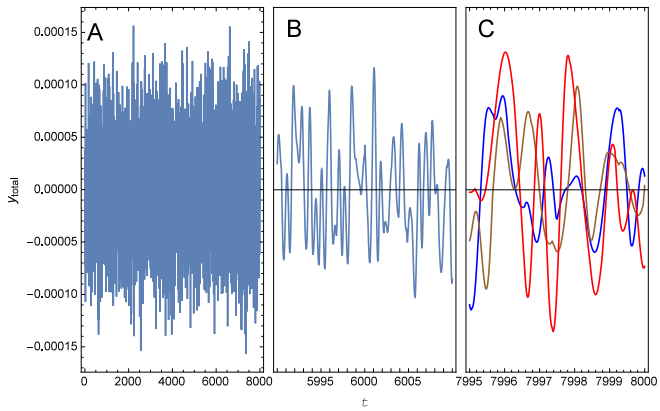

Fig. 3. Input when noise is present. The height of the BM relative to its equilibrium position is $y_{\rm total}(t) = A\cos\omega_{\rm BM}t + A_N\sum_{j=1}^{4}\cos(\omega_j t - \Phi_j)$, with $A = 3\times10^{-5}$, $\omega_{\rm BM} = 5.329$, $A_N = 3.5\times10^{-5}$, ω_j periodically randomized and Φ_j determined by continuity. A: Entire considered range. B: A range that contains the instant $t = 6000$, at which the signal is switched on. C: Three lines obtained during equivalent periods while the signal was on: the blue line describes the period $7995 < t < 8000$ and the brown (respectively red) line describes a lapse of time that preceded by 400 (respectively 3500) times $2\pi/\omega_{\rm BM}$. Our units are specified in section 3B.

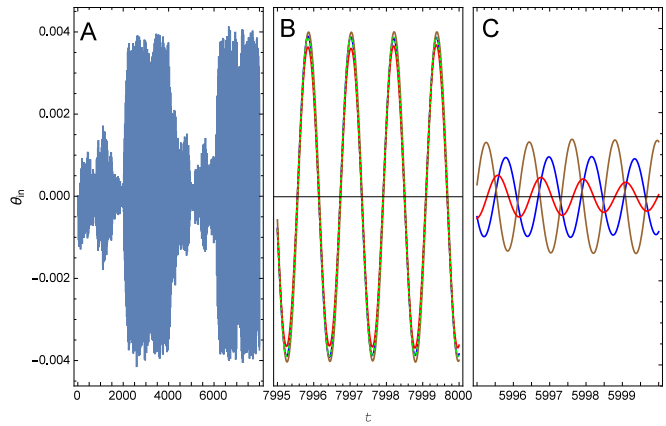

Fig. 4. Output, $\theta_{\rm in}(t)$, for the situation considered in Fig. 3. A: Entire range. B: The blue, brown and red lines correspond to the same periods of time shown in Fig. 3C; the dotted green line was obtained by dropping the contribution of noise to $y_{\rm total}(t)$. C: The three lapses of time shown in panel B have been shifted 2000 units to the left, so that they cover ranges when no signal was present.

the signal makes a significant difference. Figure 3C contains three lines: the blue line shows $y_{\rm total}(t)$ during the lapse of time indicated at the abscissa, close to $t = 8000$; the brown line refers to the values of $y_{\rm total}(t)$ at times preceding by $400\times2\pi/\omega_{\rm BM} \approx 472$, after the signal had been on during about 1500 time units, and the red line refers to times preceding by $3500\times2\pi/\omega_{\rm BM}$, close to the end of the first stage during which the signal was on. Despite the fact that the signal was identical during the three lapses of time considered, there is no obvious correlation among the three lines.

In contrast to Fig. 3A, we see in Fig. 4A that $\theta_{\rm in}$ is significantly larger when the signal is on than when it is off. The blue, brown and red lines in Fig. 4B show $\theta_{\rm in}(t)$ for the same periods of time that were considered in Fig. 3C. In this case the three lines almost coalesce, and are very close to the values of $\theta_{\rm in}(t)$ that are obtained without noise. In particular, we note that the phase of $\theta_{\rm in}(t)$ is locked to the phase of the signal.

Figure 4C shows $\theta_{\rm in}(t)$ for $5995 < t < 6000$, and also for periods of time preceding by 400 and by 3500 times $2\pi/\omega_{\rm BM}$. In the three cases, the signal was off. We learn from here that the IHB undergoes significant oscillations due to thermal fluctuations even though there is no signal. We also note that there is "ringing," i.e., oscillations are larger after the signal was on, and it takes some time until they recover the distribution expected from thermal fluctuations. Unlike the case of Fig. 4B, the phase is not locked, and wanders within a relative short time. If the brain is able to monitor the phase of $\theta_{\rm in}(t)$, an erratic phase difference between the information coming from each of the ears could be used to discard noise-induced impulses, and a continuous drift in phase difference could be interpreted as motion of the sound source.

Comparison of Figs. 3 and 4 strongly suggests one possible answer to the question of why the IHB is not attached to the TM: in this way the signal to noise ratio increases remarkably.

Additional results are reported in Section 5.

3. Analytical Procedure

A. Scope and conventions. We deal with a layer of the OoC, so that our analysis is at most two dimensional. Whenever we mention mass, force, moment of inertia, torque, or flow rate, it should be understood as mass (or force, etc.) per unit thickness of the layer. Our set of models is sufficiently simple to permit analytic integrations over space, and we will be left with a system of differential equations for functions of time, that can be solved numerically. Since these equations are nonlinear, we do not perform a Fourier analysis. There are normally three rows of outer hair cells, but we believe that the important fact is that there is more than one, and include just two outer hair cells in our explicit models.

Guided by measurements that indicate that the RL pivots as a rigid beam around the pillar cells head (23, 24), we take the origin at this pivot point. We will assume that the equilibrium positions of the RL and of the upper border of the HC lie along a straight line, that will be taken as the x-axis (that will be enviewed as "horizontal"). We will assume that below the x-axis motion is in the "vertical" direction only [although in the apical case the x-component of motion can be important (15, 25)].

By "height" of the RL, the HC, or the TM, $y_{\rm RL}(x)$, $y_{\rm HC}(x)$, and $y_{\rm T}(x)$, we will imply a position at the surface that is in contact with the endolymph. The width of the subtectorial channel is $D(x) = y_{\rm T}(x) - y_{\rm RL}(x)$ [or $y_{\rm T}(x) - y_{\rm HC}(x)$], and we will assume that in equilibrium $D(x)$ is constant and denote it by D_0. Vertical forces will be considered positive when they act upwards and angular variables will be positive when counterclockwise.

B. Common notations and units. We denote by L, $L_{\rm HC}$ and $L_{\rm T}$ the lengths of the RL, the HC, and the TM. θ will be the angle of the RL with respect to the x-axis and $\theta_{\rm in}$ the angle of the IHB with respect to the y-axis. We assume that $|\theta(t)| \ll 1$, so that the projections of the RL and the HC onto the x-axis also cover lengths L and $L_{\rm HC}$.

For an arbitrary function f of position and time, we denote $f' := \partial f/\partial x$ and $\dot f := \partial f/\partial t$.

The amplitude of a periodic, or approximately periodic,

bioRxiv preprint doi: https://doi.org/10.1101/760835; this version posted September 8, 2019. The copyright holder for this preprint (which was not certified by peer review) is the author/funder, who has granted bioRxiv a license to display the preprint in perpetuity. It is made available under aCC-BY-NC-ND 4.0 International license.

function f (not necessarily sinusoidal) will be defined as the root mean square deviation from its average,

$$|f| := \left(\int_{t_1}^{t_2} f^2(t)dt/(t_2-t_1) - \left[\int_{t_1}^{t_2} f(t)dt/(t_2-t_1) \right]^2 \right)^{1/2}, \quad [2]$$

where $t_2 - t_1$ is an integer number of periods. The absolute value of $f(t)$ at a given time will be denoted as $|f(t)|$ (with the argument written explicitly).

The unit of length will be D_0, the unit of time, D_0^2/ν, and the unit of mass, ρD_0^2, where ν and ρ are the kinematic viscosity and the density of endolymph. The expected orders of magnitude of these units are $D_0 \sim 10\mu$m, $D_0^2/\nu \sim 10^{-4}$s, and $\rho D_0^2 \sim 10^{-7}$kg/m. All our variables and parameters will be expressed in terms of these units.

4. Detailed Modelling

A. Subtectorial channel. We denote by $p(x,y,t)$ the pressure in the endolymph and by $v(x,y,t)$ the x-component of the local velocity. The flow rate in the x-direction is

$$Q(x,t) = \int_{y_{\mathrm{RL,HC}}(x)}^{y_{\mathrm{T}}(x)} v(x,y,t)dy\,. \quad [3]$$

We will assume that motions of the RL, the HC and the TM are very small in comparison to D_0, so that the limits of integration can be set as 0 and D_0 (i.e. 1 in our units). We assume that endolymph is incompressible, so that the net flow entering a region has to be compensated by expansion of that region and therefore

$$Q' = -\dot{D}\,. \quad [4]$$

Invoking incompressibility and the fact that the Reynolds number is very small, the x-component of the Navier–Stokes momentum equation can be linearized and reduced to

$$\dot{v} - v'' - \partial^2 v/\partial y^2 = -p'\,. \quad [5]$$

By means of a suitable expansion in powers of D_0/L (see *Supporting Information*) we conclude that the pressure can be taken as independent of y and obtain the approximate relation

$$Q + \dot{Q}/10 = -p'/12\,. \quad [6]$$

We assume that the only input is motion of the BM, whereas the pressure $p(L_{\mathrm{T}})$ at the exit to the SM is taken as constant. We will set $p(L_{\mathrm{T}}) = 0$, i.e., pressure in the SM will be taken equal to the pressure in the tissues below the x-axis.

B. Reticular lamina. We regard it as a straight beam. We exclude from it the CPs, that will move as independent bodies. It obeys the rotational equation of motion

$$I_{\mathrm{RL}}\ddot{\theta} = -\kappa_{\mathrm{RL}}\theta + \sum F_i x_i + F_{\mathrm{H}}L - \int_{\mathrm{RL}} p(x)xdx\,, \quad [7]$$

where I_{RL} and κ_{RL} are the moment of inertia and the rotational stiffness of the RL, F_i is the force exerted on the RL by the CP centered at $x = x_i$, F_{H} is the force exerted on the RL by the HC, and the integration is over the range $0 \le x \le L$ excluding the CPs.

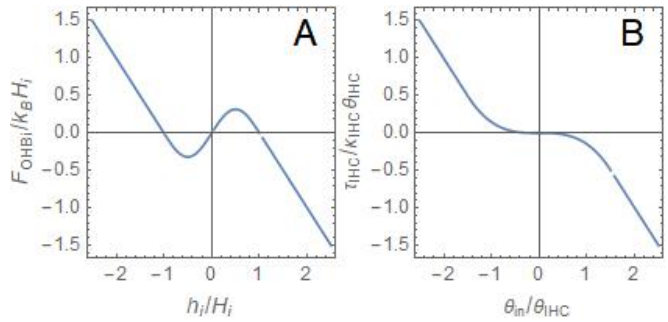

Fig. 5. A: Restoring force exerted on the CP by OHB i, as a function of the height h_i of the CP over its average value, as stipulated in Section 4E. B: Restoring torque exerted on IHB by the inner hair cell, as a function of the bundle deflection θ_{in}, as stipulated in Section 4J.

C. Cuticular plates. The CPs are the upper edges of the OHCs, where the OHBs are enrooted. In reptiles and amphibians, the cytoplasma between a CP and the surrounding RL has scarce actin filaments and little mechanical resistance (26–28). In mammals, the CP has a lip that protrudes beyond the OHC cross section and extends to tight junctions with neighboring cells. The β-actin density in the CP is much lower than that in stereocilia or in the meshwork through which stereocilia enter the plate, and is therefore expected to be relatively flexible (29). We will assume that each CP can form a bulge (or indentation) relative to the RL. The length of each CP will be ℓ and its height $y_i(x) = \theta x + b_i(1 + \cos[2\pi(x - x_i)/\ell])$, where b_i is the average height above the RL. Attributing to the CP a mass m and a position $y_i = h_i := \theta x_i + b_i$, its equation of motion is

$$m(\ddot{\theta}x_i + \ddot{b}_i) = -F_i + F_{\mathrm{OHB}i} - F_{\mathrm{OHC}i} - \int_{x_i-\ell/2}^{x_i+\ell/2} p(x)dx\,, \quad [8]$$

where $F_{\mathrm{OHB}i}$ is the force exerted by the hair bundle and $F_{\mathrm{OHC}i}$ the tension of the cell. We set $F_i = k_{\mathrm{CP}}b_i + \beta_{\mathrm{CP}}\dot{b}_i$, where k_{CP} and β_{CP} are a restoring and a damping coefficient.

D. Tectorial membrane. We assume that it remains in a constant position, $y_{\mathrm{T}}(x) = 1$.

E. Outer hair bundles. We assume that they exert a force that is a function of the tilt angle, which in turn is a function of h_i. We mimic the measured force (31), which has an unstable central region, by means of the expression

$$F_{\mathrm{OHB}i} = \begin{cases} -k_B[h_i - \mathrm{sgn}(h_i)H_i] & |h_i(t)| \ge H_i \\ k_B H_i \sin(\pi h_i/H_i)/\pi & |h_i(t)| < H_i\,. \end{cases} \quad [9]$$

k_B defines the stiffness (we will write k_{Bolt} for Boltzmann's constant) and H_i the range of the unstable region. $F_{\mathrm{OHB}i}(h_i)$ is shown in Fig. 5.

Taking $F_{\mathrm{OHB}i}$ as a function of h_i implies that the work performed by bundle motility vanishes for a complete cycle.

F. Outer hair cells. We envision an OHC as a couple of objects, each with mass m, connected by a spring. One object is located at the CP and the other at the boundary with the Deiter cell (DC). A special feature of the spring is that its relaxed length can vary. We denote by c_i the contraction of the cell with respect to its average length, and by s_i the height

DRAFT

bioRxiv preprint doi: https://doi.org/10.1101/760835; this version posted September 8, 2019. The copyright holder for this preprint (which was not certified by peer review) is the author/funder, who has granted bioRxiv a license to display the preprint in perpetuity. It is made available under aCC-BY-NC-ND 4.0 International license.

of the lower object with respect to its average position. We assume that the tension of the OHC has the form

$$F_{\mathrm{OHC}i} = k_C(\theta x_i + b_i - s_i + c_i) + \beta_C(\dot\theta x_i + \dot b_i - \dot s_i)\,, \quad [10]$$

with k_C and β_C positive constant parameters.

The value of c_i is controlled by the inclination of the hair bundle. We assume that h_i, scaled with the length H_i, acts as a "degree of excitation," so that c_i increases with h_i/H_i. Since there must be a maximum length, Δ, by which an OHC can contract, and we expect that contraction should saturate for too large deviations of the OHB from its average position, we take this saturation into account by writing

$$c_i = \Delta \tanh(h_i/H_i)\,. \quad [11]$$

The degree of excitation h_i/H_i may be identified with $Z(X - X_0)/2k_{\mathrm{Bolt}}T$ in Eq. 3 of (30).

Since c_i is not a function of the distance between the objects on which $F_{\mathrm{OHC}i}$ acts, $F_{\mathrm{OHC}i}$ *can* perform non vanishing work in a complete cycle, as will be spelled out in Section 5D.

G. Deiter cells. We model a DC as a massless spring that connects the lower object in the OHC to the BM (the mass of the DC is already lumped into m). We also include dynamic friction between adjacent lower objects, that encourages oscillation in phase. Denoting by y_{BM} the height of the BM above its average position, we write

$$m\ddot s_i = F_{\mathrm{OHC}i} + k_{\mathrm{D}i}(y_{\mathrm{BM}} - s_i) - \beta_{\mathrm{D}i}\dot s_i + \beta_{\mathrm{D}ij}(\dot s_j - \dot s_i)\,, \quad [12]$$

where DC j is adjacent to DC i. Since DC are longer for larger x, $k_{\mathrm{D}i}$ and $\beta_{\mathrm{D}i}$ could depend on i.

H. Hensen cells. We model the HC as a strip with parabolic shape of evenly distributed mass m_{H}, with its left extreme tangent to the RL and the other extreme pinned at $(x, y) = (L + L_{\mathrm{HC}}, 0)$. These requirements impose $y_{\mathrm{HC}}(x) = \theta[x - (L + L_{\mathrm{HC}})(x - L)^2/L_{\mathrm{HC}}^2]$. The torque exerted on the HC with respect to the pinning point is $F_{\mathrm{H}}L_{\mathrm{HC}} + \int_L^{L+L_{\mathrm{HC}}} p(x)(L + L_{\mathrm{HC}} - x)dx$, and equals the time derivative of the HC angular momentum, $-(m_{\mathrm{H}}/L_{\mathrm{HC}})\int_L^{L+L_{\mathrm{HC}}} \ddot y_{\mathrm{HC}}(L+L_{\mathrm{HC}}-x)dx$, leading to

$$F_{\mathrm{H}} = -\frac{m_{\mathrm{H}}}{12}(5L+L_{\mathrm{HC}})\ddot\theta - \frac{1}{L_{\mathrm{HC}}}\int_L^{L+L_{\mathrm{HC}}} p(x)(L+L_{\mathrm{HC}}-x)dx\,. \quad [13]$$

Since we assume that the pressure vanishes in the SM, we replace the upper limit in the integral with the end of the subtectorial channel. We will take this end over the position where the HC has maximum amplitude, namely, $L_{\mathrm{T}} = L + L_{\mathrm{HC}}^2/2(L + L_{\mathrm{HC}})$.

I. Inner sulcus. We assume that the pressure p_{in} in the inner sulcus (IS) is uniform and proportional to the increase of area (volume per thickness) with respect to the relaxed IS. We write

$$\dot p_{\mathrm{in}} = -CQ(0)\,. \quad [14]$$

C is some average value of the Young modulus divided by the area (in the xy-plane) of the soft tissue that coats the IS and $Q(0)$ is the flow rate for $x = 0$.

J. Inner bundle. We locate it at $x = 0$ and assume that its length is almost 1. The force exerted by viscosity on a segment of the IHB between y and $y + dy$ is proportional to the relative velocity of endolymph with respect to the segment, and we denote it by $\mu[Q(0) + y\dot\theta_{\mathrm{in}}]dy$, where μ is a drag coefficient and we have replaced $v(y)$ by its average. On average, the force per unit length is $\mu[Q(0) + \dot\theta_{\mathrm{in}}/2]$. We identify this force with the pressure difference and write

$$p_{\mathrm{in}} - p(0) = \mu[Q(0) + \dot\theta_{\mathrm{in}}/2]\,. \quad [15]$$

$p(0)$ is the pressure at $x = 0$.

The torque exerted by viscosity is $-\mu[Q(0)/2 + \dot\theta_{\mathrm{in}}/3]$. We assume that the moment of inertia of the bundle is negligible and write $\tau_{\mathrm{IHC}} - \mu[Q(0)/2 + \dot\theta_{\mathrm{in}}/3] = 0$, with τ_{IHC} the torque exerted by the cell. We assume that the inner hair cell does not rotate, and τ_{IHC} is a function of θ_{in}. It seems reasonable to assume that the IHB does not have a central range with negative stiffness as the OHB, since it could cause sticking of the bundle at any of the angles at which stiffness changes sign. We will assume that, as a remnant of the OHB negative stiffness, $\partial\tau_{\mathrm{IHC}}/\partial\theta_{\mathrm{in}}$ vanishes at $\theta_{\mathrm{in}} = 0$ [alike Fig. 1(C) in (32)], and write

$$\tau_{\mathrm{IHC}} = \begin{cases} -\kappa_{\mathrm{IHC}}[\theta_{\mathrm{in}} - \mathrm{sgn}(\theta_{\mathrm{in}})\theta_{\mathrm{IHC}}] & |\theta_{\mathrm{in}}(t)| \geq 3\theta_{\mathrm{IHC}}/2 \\ -4\kappa_{\mathrm{IHC}}\theta_{\mathrm{in}}^3/27\theta_{\mathrm{IHC}}^2 & |\theta_{\mathrm{in}}(t)| < 3\theta_{\mathrm{IHC}}/2\,. \end{cases} \quad [16]$$

τ_{IHC} is a smooth function of θ_{in} and the parameters κ_{IHC} and θ_{IHC} determine its size and the extension of the low stiffness region. $\tau_{\mathrm{IHC}}(\theta_{\mathrm{in}})$ is shown in Fig. 5.

We assume that the rate of impulses passed to the auditory nerve is an increasing function of the amplitude $|\theta_{\mathrm{in}}|$.

K. Basilar membrane. In the absence of noise, we assume that the BM drives the lower ends of the DCs, all of them by the same amount, $y_{\mathrm{BM}} = A\cos\omega_{\mathrm{BM}}t$.

L. Noise. We mimic white noise by adding to y_{BM} in Eq. [12] four sinusoidal additions $A_{\mathrm{N}}\cos(\omega_j t - \Phi_j)$, where the frequencies ω_j are randomly taken from a uniform distribution in the range $0 \leq \omega_j \leq 2\omega_{\mathrm{BM}}$. ω_1 (respectively ω_2, ω_3, ω_4) is re-randomized at periods of time 0.7 (repectively 0.9, 1.1, 1.3). The values of Φ_j are initially random, and afterwards are taken so that $A_{\mathrm{N}}\cos(\omega_j t - \Phi_j)$ is continuous. A_{N} is taken so that the average energy added to the DC (assuming that the considered layer has thickness D_0) is of the order of $k_{\mathrm{Bolt}}T \sim 4.2\times10^{-21}$J. The initial values of most variables are taken from normal distributions appropriate for average energies of the order of $0.5k_{\mathrm{Bolt}}T$ per degree of freedom; we assume that these initial values become unimportant after a short time.

M. Procedure. Equations [4]–[16] are integrated as will be now described. We assume that the variables $p(x,t)$, $Q(x,t)$, $\theta(t)$, $b_i(t)$, $s_i(t)$, $\theta_{\mathrm{in}}(t)$, $p_{\mathrm{in}}(t)$, and whenever relevant also their time derivatives, are known at a given time t. To find their values at a subsequent time $t + dt$, we integrate equation [7] to obtain $\theta(t + dt)$. Then $b_i(t + dt)$ and $s_i(t + dt)$ can be obtained by integrating equations [8] and [12], taking into account the constitutive relations [9], [10] and [11]. Given θ and b_i we can evaluate $y_i(t+dt)$, and from it the time derivative of D at that time step. Using equation [14], p_{in} can be eliminated from equation [15]. Then, using $p(0,t)$, and relation [16], equations [15] and the torque equation can be solved simultaneously for

DRAFT

bioRxiv preprint doi: https://doi.org/10.1101/760835; this version posted September 8, 2019. The copyright holder for this preprint (which was not certified by peer review) is the author/funder, who has granted bioRxiv a license to display the preprint in perpetuity. It is made available under aCC-BY-NC-ND 4.0 International license.

Table 1. Parameters used in our calculations

Parameter	L	L_H	x_1	x_2	ℓ	m	m_H	I_{RL}	κ_{RL}	k_{CP}	β_{CP}	k_C	β_C	k_{D1}	k_{D2}	β_{D1}	β_{D2}	β_{D12}	k_B	H_1	H_2	κ_{IHC}	θ_{IHC}	C	μ
Value	10	10	3	7	2	10	120	2×10^3	10^3	10^2	3	50	43	400	400	3	3	3	10	6.5×10^{-3}	5×10^{-3}	10	5×10^{-3}	2	10
Definition	3B	3B	4C	4C	4C	4C	4H	4B	4B	4C	4C	4F	4F	4G	4G	4G	4G	4G	4E	4E	4E	4J	4J	4I	4J

We assume that the maximal contraction of the OHC takes its bifurcation value, which for these parameters is $\Delta_c = 0.254$. The third row indicates the section where the symbol is defined. The system of units is defined in Section 3B.

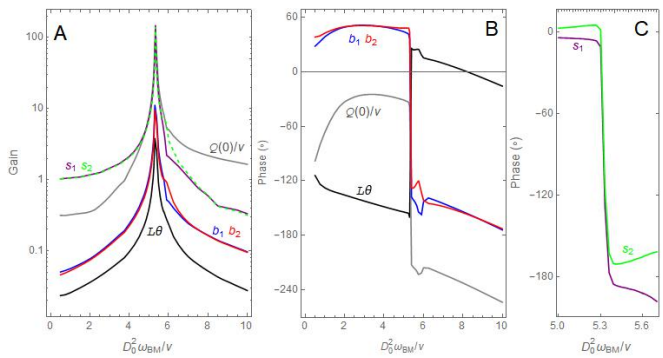

Fig. 6. Amplitude and phase of several variables, relative to the input $y_{\mathrm{BM}} = 10^{-4} D_0 \cos\omega_{\mathrm{BM}} t$. A: Amplitude, as defined in Eq. [2]. For visibility, s_2 is depicted by a dashed line. B: Phase by which the variable precedes the input. Phases that differ by an integer number of cycles are taken as equivalent. The phase of a variable is defined as the phase of its first harmonic (see *Supporting Information*). C: Phases of s_1 and s_2 near the resonance. Here and in the following figures noise has been neglected.

$Q(0)$ and θ_{in} to obtain their values at $t + dt$. This enables the space integration of [4] for Q and then of [6] for p to obtain all the variables at time $t + dt$. The technical details can be accessed from the *Supporting Information*.

N. Parameters. Clearly, parameters vary among species, among individuals, and along the cochlea. We tried to set parameters of reasonable orders of magnitude. When available, we took values from the literature. When forced to guess, we chose values guided by several inklings and criteria, such as large response, fast stabilization, similar amplitudes of $b_1(t)$ and $b_2(t)$, avoidance of beating, resonance frequency in a reasonable range, etc. Some of the parameters have almost no influence. The parameters we took are listed in Table 1.

5. Further Results and Discussion

A. Why it works. We can show (to be submitted elsewhere) that a system of two particles, with a "spring" force between them of the form [10] that depends on the position of one of the particles, and with appropriate restoring and damping coefficients, behaves as a critical oscillator. The critical control parameter of this "bare" oscillator (with the same parameters used in Table 1) is considerably smaller than the value of Δ_c that we found for the OoC. These bare oscillators (one for each OHC) drive the entire OoC.

B. Motion of each component. Figure 6 shows the amplitudes and phases of $Q(0)/\nu$, $b_{1,2}$, $s_{1,2}$ and $L\theta$ for a broad range of input frequencies. b_1 and b_2, and likewise s_1 and s_2, nearly coincide, except for a small range of frequencies slightly above the resonance, where motion in the first OHC is considerably smaller than in the second. $L|\theta|$ is roughly three times smaller than $|b_{1,2}|$ and θ is nearly in anti-phase with $b_{1,2}$ (lags by $\sim 200°$). The opposite motions of the RL and the CPs may be attributed to incompressibility and to our assumption of a rigid TM, so that when one of them goes up the other has to go down. $Q(0)$ typically lags behind $b_{1,2}$ by $\sim 80°$; following the incompressibility argument, $Q(0)$ is positive when the sum of the subtectorial volumes taken by the CPs, the RL and the HC is decreasing. All the variables undergo a 180° change when crossing the resonance.

Separate motion of the CPs and the RL has not been detected experimentally. We could argue that the lateral spacial resolution of the measuring technique did not distinguish between the CPs and the surrounding RL, so that the measured motion corresponds to some average, but the spot size reported in (23) (less than a μm) excludes this possibility. In the case of (23) there was electrical simulation, and no input from the BM. The most likely possibility is that the TM recedes when the CPs go up, so that the RL does not have to recede and is mainly pulled by the CPs.

A marked difference between (14) and Fig. 6 is the absence of phase inversion when crossing the resonance. A possible explanation could be that the maximum gain (amplitude of RL motion divided by BM motion) occurs at a frequency that lies above the range considered in Fig. 5 of (14). A sharp decrease of the phase of the RL relative to the BM occurs in (22).

C. Limitations of the models. We have found a possible simplified description of how the components of the OoC could collaborate to amplify input vibrations, with the result of increased frequency selectivity, amplitude compression, and ability to uncover a weak signal from thermal noise. This does not necessarily mean that the activity of each component of the OoC in a mammal actually follows our equations: a well known feature of critical phenomena is that the same common behavior can be obtained for models with different details (33–35).

Obviously, by overlooking degrees of freedom such as fluid flow in the longitudinal direction, interaction of the studied layer with its neighbors, pressure variations in the SM, and flexibility of the TM, and by representing mass distributions by point objects, our description of the OoC is doomed to be a caricature rather than a portrait. What our results show is that the ignored degrees of freedom are not essential for the functioning of the OoC. On the other hand, these features could be important in the description of the activity of the OoC as it happens to occur in nature. Most probably, some of our models are close to reality, while others have to be reformulated in light of observations.

D. Mechanical energy transfer. The power delivered by electromotility of OHC i is $-k_C c_i(\dot{h}_i - \dot{s}_i)$. Using Eq. [11] and dropping the terms that give no contribution through a complete cycle, the work performed by electromotility during a

DRAFT

bioRxiv preprint doi: https://doi.org/10.1101/760835; this version posted September 8, 2019. The copyright holder for this preprint (which was not certified by peer review) is the author/funder, who has granted bioRxiv a license to display the preprint in perpetuity. It is made available under aCC-BY-NC-ND 4.0 International license.

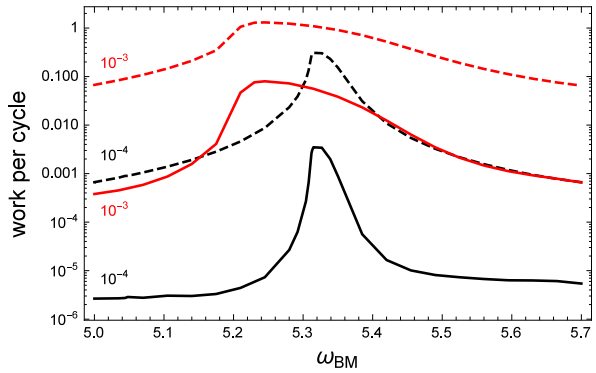

Fig. 7. Work performed during a cycle for frequencies close to resonance. The dashed lines refer to the work delivered by electromotility, $W_{\rm OHC}$, and the continuous lines to the work taken from the BM, $-W_{\rm DC1} - W_{\rm DC2}$. $y_{\rm BM} = AD_0 \cos\omega_{\rm BM} t$ and the value of A is shown next to each line.

complete cycle is

$$W_{\rm OHC} = k_C \Delta \sum_{i=1}^{2} \int \tanh(h_i/H_i)\dot{s}_i dt\,, \qquad [17]$$

where integration involves a complete cycle. Since both h_i and s_i undergo a phase inversion when crossing the resonance, the sign of $W_{\rm OHC}$ remains unchanged.

Similarly, the work per cycle performed by DC i on the BM is

$$W_{{\rm DC}i} = -Ak_{Di}\omega_{\rm BM} \int s_i \sin\omega_{\rm BM} t\, dt\,. \qquad [18]$$

Since the speed of the traveling wave vanishes at the characteristic place of the cochlear partition, quite a few cycles occur as the traveling wave passes through a layer of the OoC close to a position that corresponds to its frequency.

$W_{{\rm DC}i} > 0$ if and only if the phase of s_i is in the range between 0° and 180° (or equivalent). We see from Fig. 6C that very near the resonance $W_{\rm DC1}$ and $W_{\rm DC2}$ are both negative, indicating that the OoC takes mechanical energy from the BM. Below this region (but still in the range shown in this figure), $W_{\rm DC1} < 0$, $W_{\rm DC2} > 0$, and the opposite situation occurs above this region.

Figure 7 shows the values of these works close to the resonance frequencies, for $A = 10^{-4}$ and $A = 10^{-3}$. Most of the energy required for motion in the OoC is supplied by electromotility, and a small fraction is taken from the BM. We note that $W_{\rm DC1} + W_{\rm DC2} < 0$ in the entire range shown in the figure. Since in our set of models $W_{\rm DC1} + W_{\rm DC2}$ is the only exchange of mechanical energy between the considered layer of the OoC and its surroundings, this result implies that mechanical energy is taken from the traveling wave, leading to attenuation. Since it is experimentally known that the traveling wave is amplified for frequencies below resonance, our models will have to be upgraded.

E. Time dependence of the output. Figure 8 shows $\theta_{\rm in}(t)$ for $A = 10^{-5}$ and frequencies near resonance. The blue envelope was obtained at resonance frequency, the pink envelope at $\omega_{\rm BM} = 5.34$ and the green envelope at $\omega_{\rm BM} = 5.32$. In the case of resonance, the output amplitude raises monotonically until a terminal value is attained. Out of resonance, the amplitude starts increasing at the same pace as at resonance,

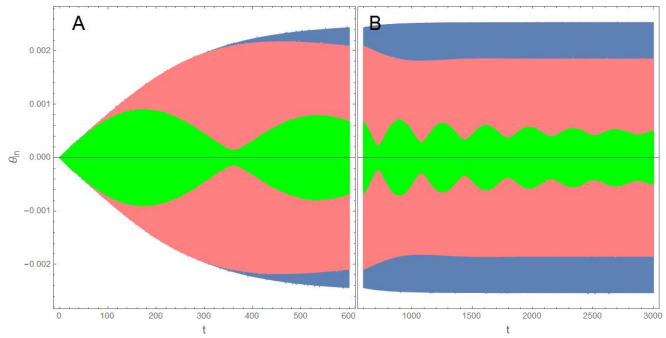

Fig. 8. Angle of the IHB as a function of time in response to $y_{\rm BM} = 10^{-5} D_0 \cos\omega_{\rm BM} t$. Blue: resonance frequency, $\omega_{\rm BM} = \omega_R = 5.334$; pink: $\omega_{\rm BM} = 5.34$; green: $\omega_{\rm BM} = 5.32$. A: $0 \le t \le 600$. B: $t \ge 600$.

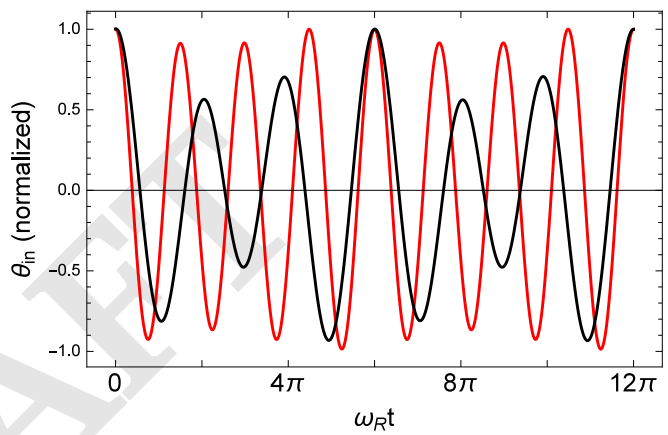

Fig. 9. $\theta_{\rm in}(t)$ during a short period of time. Black: $\omega_{\rm BM} = (2/3)\omega_R$; red: $\omega_{\rm BM} = (4/3)\omega_R$. t is the time elapsed after a maximum of $\theta_{\rm in}$, roughly 4000 time units after the input was set on. $A = 10^{-5}$.

overshoots its final value, and then oscillates until the final regime is established. This initial behavior has the effect of sending a fast alarm from several layers of the OoC telling that something is happening, before it is possible to discern the precise frequency.

In contrast with a forced damped harmonic oscillator, when out of resonance, motion of the OoC does not assume the frequency of the input even after a long time, but is rather the superposition of two modes, one with the input frequency $\omega_{\rm BM}$, and the other with the resonance frequency ω_R. If $\omega_{\rm BM} = (n_1/n_2)\omega_R$, where $n_{1,2}$ are mutually prime integers, then the motion has period $2n_2\pi/\omega_R$. Figure 9 shows $\theta_{\rm in}(t)$ for $\omega_{\rm BM} = (2/3)\omega_R$ and for $\omega_{\rm BM} = (4/3)\omega_R$.

F. Nonlinearity. We studied the deviation from sinusoidality of $\theta_{\rm in}(t)$ at resonance frequency, when the periodic regime is established. Writing $\theta_{\rm in}(t) = \sum_{n=0}^{\infty} a_n \cos[n(\omega_{\rm BM} t + \phi_n)]$, the even harmonics vanish. Taking the origin of time such that $\phi_1 = 0$, we found the values in Table 2.

G. Additional mechanisms. According to our models, the reason for fluid flow at the IHB region is the vertical motion of the CPs, the RL and the HC, but other drives are also possible (36, 37). Flow could be due to shear between the TM and the RL, squeezing of the IS, or deviation of part of the RL from

bioRxiv preprint doi: https://doi.org/10.1101/760835; this version posted September 8, 2019. The copyright holder for this preprint (which was not certified by peer review) is the author/funder, who has granted bioRxiv a license to display the preprint in perpetuity. It is made available under aCC-BY-NC-ND 4.0 International license.

Table 2. $\theta_{\rm in} \approx a_1 \cos\omega_{\rm BM} t + a_3 \cos[3(\omega_{\rm BM} t + \phi_3)] + a_5 \cos[5(\omega_{\rm BM} t + \phi_5)]$

A	a_1	a_3/a_1	ϕ_3	a_5/a_1	ϕ_5
10^{-3}	1.25×10^{-2}	0.0344	0.70	0.0050	-0.34
10^{-4}	5.75×10^{-3}	0.0097	0.67	0.0001	-0.51
10^{-5}	2.54×10^{-3}	0.0017	0.66	0.0000	

A is the peak value of the input and $\omega_{\rm BM}$ equals the resonance frequency. $\phi_{3,5}$ are the phases with respect to the first harmonic of $\theta_{\rm in}$.

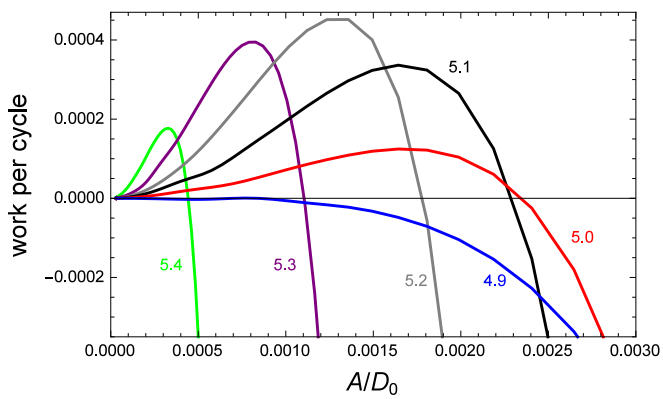

Fig. 10. Work performed on the BM as a function of the amplitude of the BM oscillations, for the case considered in Section 5H. The parameter $\omega_{\rm BM}$ is shown next to each curve. The travelling wave is amplified if this work is positive and attenuated if it is negative. After many cycles, the amplitude of the BM oscillations would be largest for $\omega_{\rm BM} \approx 5.0$

the x-axis, implying an x-component of its velocity when it rotates.

For comparison of the relative importance of each of these mechanisms, we examine the peak values that we obtained for $A = 10^{-4}$ at resonance frequency. For $Q(0)$, which in our units equals the average over y of $v(y)$, we found $\sim 2 \times 10^{-2}$. The vertical velocity of the CPs is less than 10^{-2}. From here we expect that the shear velocity of the RL with respect to the TM will be less than that, and the average fluid velocity even smaller.

The peak value of $\dot{\theta}$ is $\sim 5 \times 10^{-4}$. Assuming that the length of the RL that invades the IS is $\sim 4D_0$, squeezing would cause a flux rate of $\sim 10^{-3}$. It therefore seems that the mechanism that we have considered is the most important. In the case of a flexible TM, θ would be larger and the flux due to squeezing would grow accordingly.

H. Variations of parameters. We will consider an example in which varying a parameter can qualitatively modify the behavior of the OoC. In this example, we raise k_{D2} by 10%, to 440. With this change, Δ_c becomes 0.290 and ω_c, 5.506. An increase of Δ_c implies additional effort of the OHCs, which have to undergo larger contractions. This extra investment is rewarded by the possibility to amplify the traveling wave in some ranges, as shown in Fig. 10. In the limit that the traveling wave spends a very large number of cycles while passing a region with parameters similar to those of the layer we consider, it will be either amplified or attenuated, until it reaches the amplitude for which the work performed on the BM vanishes. In general, the initial amplitude will be shifted towards this limiting value.

We do not claim that this is actually the mechanism by which the OHCs transfer energy to the BM; we just illustrate how this transfer can be manipulated by a suitable adjustment of parameters. Conceivably, the advantage of having several OHCs per layer (rather than a single stronger OHC) is the increase of the number of degrees of freedom, that might be necessary to permit coalescence, or at least closeness, of the tuning at the BM with that of the transfer from the BM to the IHB.

I. Variations of the models.

I.1. Bundle motility. Bundle motility can be eliminated from the model by setting $H_i = 0$ in Eq. 9 (but not in [11]). We still obtain that the OoC can behave as a critical oscillator, but the critical value for OHC contraction rises to $\Delta_c = 0.262$. Our conclusion is thus that bundle motility helps attainment of critical oscillator behavior, but is not essential.

I.2. Asymmetric contraction. OHCs contract by a greater amount when depolarized than what they elongate when hyperpolarized. For simplicity, this property was overlooked in Eq. 11 [which corresponds to the assumption that there are equal probabilities for open and for closed channels (30)]. We have found that, with this symmetric dependence, the OoC is unable to demodulate the envelope of a signal, as it occurs in (21). The study of a model in which c_i is an asymmetric function of h_i/H_i is underway.

I.3. Removal of the HC. This was done by setting $L_{\rm T} = L$ and $F_{\rm H} = 0$. The bifurcation value of Δ increased to $\Delta_c = 0.273$, suggesting that an advantage of the HC is reduction of the value of contraction required to achieve criticality. The comparison may be somewhat biased by the fact that our parameters were optimized with the HC included.

J. Bottom line. We have built a framework that enables to test many possibilities for the mechanical behavior of the components of the OoC. The models we used imply that even by taking the basilar membrane motion as an input, the OoC behaves as a critical oscillator, thus providing a second filter. This filter enhances frequency selectivity, improves the signal to noise ratio, and exhibits self-oscillations. This framework can be used to explore and theoretically predict different effects that would be hard to observe experimentally. In particular, applying the basic models developed here enabled us to obtain features that are compellingly akin to those observed in the real OoC.

ACKNOWLEDGMENTS. We are indebted to David Furness, Karl Grosh, James Hudspeth and Yehoash Raphael for their answers to our inquiries.

References.

1. Robles L, Ruggero MA (2001) Mechanics of the Mammalian Cochlea. *Physiol Rev* **81** 1305–1352
2. Hudspeth AJ (2008) Making an Effort to Listen: Mechanical Amplification in the Ear. *Neuron* **59** 530–545
3. Puria S, C R Steele CR (2008) Mechano-Acoustical Transformations.The senses: A comprehensive reference, eds Basbaum AI et al (Academic, NY) Vol 3, pp 166–201
4. Duifhuis H (2012) Cochlear Mechanics (Springer,NY)
5. Hudspeth AJ (2014) Integrating the active process of hair cells with cochlear function. *Nat Rev Neurosci* **15** 600–614
6. Reichenbach T, Hudspeth AJ (2014) The physics of hearing: fluid mechanics and the active process of the inner ear. *Rep Prog Phys* **77** 076601
7. Manley GA, Gummer AW, Popper AN, Fay RR, eds (2017) Understanding the Cochlea (Springer, Cham)

DRAFT

bioRxiv preprint doi: https://doi.org/10.1101/760835; this version posted September 8, 2019. The copyright holder for this preprint (which was not certified by peer review) is the author/funder, who has granted bioRxiv a license to display the preprint in perpetuity. It is made available under aCC-BY-NC-ND 4.0 International license.

8. von Békésy G (1960) Experiments in Hearing (McGraw Hill,NY)
9. Peterson LC, Bogert BP (1950) A Dynamical Theory of the Cochlea. *J Acoust Soc Am* **22** 369—381
10. Evans EF, Wilson JP (1975) Cochlear tuning properties: concurrent basilar membrane and single nerve fiber measurements. *Science* **190** 1218–1221
11. Allen JB, Neely ST (1992) Micromechanical models of the cochlea. *Physics Today* **45** 40–47
12. Gummer AW, Hemmert W, Zenner (1996) Resonant tectorial membrane motion in the inner ear: Its crucial role in frequency tuning. *Proc Natl Acad Sci USA* **93** 8727-8732
13. Narayan SS, Temchin AN, Recio A, Ruggero MA (1998) Frequency Tuning of Basilar Membrane and Auditory Nerve Fibers in the Same Cochleae. *Science* **282** 1882–1884
14. Chen F, Zha D, Fridberger A, Zheng J, Choudhury N, Jaques SL, Wang RK, Shi X, Nutall AL (2011) A differentially amplified motion in the ear for near-threshold sound detection. *Nat Neurosci.* **14** 770–774
15. Lee HY, Raphael PD, Xia A, Kim J, Grillet N, Applegate BE, Ellerbee Bowden AK, Oghalai JS (2016) Two-Dimensional Cochlear Micromechanics Measured In Vivo Demonstrate Radial Tuning within the Mouse Organ of Corti. *J Neurosci* **36** 8160-8173
16. Ramamoorthy S, Deo NV, Grosh K (2007) A mechano-electro-acoustical model for the cochlea: Response to acoustic stimuli. *J Acoust Soc Am* **5** 2758–2773
17. Ni G, Elliott SJ, Baumgart J (2016) Finite-element model of the active organ of Corti. *J R Soc Interface* **13**: 20150913
18. Sasmal A, Grosh K (2019) Unified cochlear model for low- and high-frequency mammalian hearing. *Proc Natl Acad Sci USA* **116** 13983-13988
19. Johnstone BM, Patuzzi R, Yates GK (1986) Basilar membrane measurements and the travelling wave. *Hearing Research* **22** 147–153
20. Ruggero MA, Rich NC, Recio A, Narayan SS, Robles S (1997) Basilar-membrane responses to tones at the base of the chinchilla cochlea. *J Acoust Soc Am* **101** 2151–2163
21. Nuttall AL, Ricci AJ, Burwood G, Harte JM, Stenfelt S, Cayé-Thomasen P, Ren T, Ramamoorthy S, Zhang Y, Wilson T, Lunner T, Moore BCJ, Fridberger A, (2018) A mechanoelectrical mechanism for detection of sound envelopes in the hearing organ. *Nature Commun* **9**: 4175
22. Ren T, He W, Kemp D (2016) Reticular lamina and basilar membrane vibrations in living mouse cochleae. *Proc Natl Acad Sci USA* **113** 9910–9915
23. Nowotny M, Gummer AW (2011) Vibration responses of the organ of Corti and the tectorial membrane to electrical stimulation. *J Acoust Soc Am* **130** 3852–3872
24. Richter C-P, Quesnel A (2006) Stiffness properties of the reticular lamina and the tectorial membrane as measured in the gerbil cochlea, Auditory Mechanisms: Processes and Models, eds Nutall AL, Ren T, Gillespie P, Grosh K, de Boer E (World Scientific, Singapore) pp 70–78
25. Ciganović N, Warren RL, Keçeli B, Jacob S, Fridberger A, Reichenbach T (2018) Static length changes of cochlear outer hair cells can tune low-frequency hearing. *PLoS Comput Biol* **14** e1005936
26. Tilney LG, Derosier DJ, Mulroy MJ (1980) The organization of actin filaments in the stereocilia of cochlear hair cells. *J Cell Biol* **86** 244–259
27. Raphael Y, Athey BD, Wang Y, Lee MK, Altschuler RA (1994) F-actin, tubulin and spectrin in the organ of Corti: comparative distribution in different cell types and mammalian species. *Hear Res* **76** 173-187
28. Kachar B, Battaglia A, Fex J (1997) Compartmentalized vesicular traffic around the hair cell cuticular plate. *Hear Res* **107** 102–112
29. Furness DN, Mahendrasingam S, Ohashi M, Fettiplace R, Hackney CM (2008) The dimensions and composition of stereociliary rootlets in mammalian cochlear hair cells: comparison between high- and low-frequency cells and evidence for a connection to the lateral membrane. *J Neuroscience* **28** 6342-6353
30. Fettiplace R, Kim KK (2014) The physiology of mechanoelectrical transduction channels in hearing. *Physiol Rev* **94** 951–986
31. Martin P, Mehta AD and Hudspeth AJ (2000) Negative hair-bundle stiffness betrays a mechanism for mechanical amplification by the hair cell. *Proc Natl Acad Sci USA* **97** 12026–31
32. Tinevez J-Y, Jülicher F, Martin P (2007) Unifying the Various Incarnations of Active Hair-Bundle Motility by the Vertebrate Hair Cell. *Biophys J* **93** 4053–4067
33. Hohenberg PC, Halperin BI (1977) Theory of dynamic critical phenomena. *Rev Mod Phys* **49** 435–479
34. Duke T, Jülicher F (2008) Critical Oscillators as Active Elements in Hearing. Active Processes and Otoacoustic Emissions, Springer Handbook of Auditory Research, eds Manley GA, Popper AN, Fay RR (Springer, New York), pp 63–92
35. Hudspeth AJ, Jülicher F, Martin P (2010) A critique of the critical cochlea: Hopf—a bifurcation—is better than none. *J Neurophysiol* **104** 1219–1229
36. Nowotny M, Gummer AW (2006) Nanomechanics of the subtectorial space caused by electromechanics of cochlear outer hair cells. *Proc Natl Acad Sci USA* **103** 2120–2125
37. Guinan JJ Jr (2012) How are inner hair cells stimulated? Evidence for multiple mechanical drives. *Hearing Research* **292** 35–50

DRAFT

bioRxiv preprint doi: https://doi.org/10.1101/760835; this version posted September 8, 2019. The copyright holder for this preprint (which was not certified by peer review) is the author/funder, who has granted bioRxiv a license to display the preprint in perpetuity. It is made available under aCC-BY-NC-ND 4.0 International license.

Supplementary Information for

Anatomic set of mechanical models for the organ of Corti

Jorge Berger and Jacob Rubinstein

J. Berger
E-mail: jorge.berger@braude.ac.il

This PDF file includes:

Supplementary text: background, development, discussion and estimates for required equations and definitions
Computer code
Figs. S1 to S2
References for SI reference citations

bioRxiv preprint doi: https://doi.org/10.1101/760835; this version posted September 8, 2019. The copyright holder for this preprint (which was not certified by peer review) is the author/funder, who has granted bioRxiv a license to display the preprint in perpetuity. It is made available under aCC-BY-NC-ND 4.0 International license.

Fluid flow in a narrow channel with small rapid wall motion

The channel is defined by $T = \{(x,y)| \quad 0 < x < L,\ \xi(x,t) < y < D_0\}$. The flow problem is characterized by three nondimensional parameters:

$$\varepsilon = D_0/L, \quad \zeta = D_0^2\omega/\nu, \quad \xi/D_0 = O(\delta), \tag{S1}$$

where ω is the oscillation period (in time) of ξ, and $\nu \sim 1\,\mathrm{mm}^2/\mathrm{s}$ is the kinematic viscosity. Typical values for the length parameters above are

$$D_0 \sim 5\,\mu\mathrm{m}, \quad L \sim 50\,\mu\mathrm{m}, \quad \xi \sim 5\,\mathrm{nm}.$$

Thus, $\varepsilon \sim 0.1$, while $\delta \sim 10^{-3}$. We shall work under the canonical scaling $\zeta = \alpha\varepsilon$, where $\alpha = O(1)$.

The fluid velocity (v,u) and pressure p satisfy the time-dependent Stokes equation:

$$\nu\Delta v = \frac{1}{\rho}\frac{\partial p}{\partial x} + \frac{\partial v}{\partial t}, \tag{S2}$$

$$\nu\Delta u = \frac{1}{\rho}\frac{\partial p}{\partial y} + \frac{\partial u}{\partial t}, \tag{S3}$$

$$\frac{\partial v}{\partial x} + \frac{\partial u}{\partial y} = 0. \tag{S4}$$

Here Δ is the Laplacian operator. No-slip boundary conditions are assumed on the channel's lateral boundary.

To convert the problem to a nondimensional formulation we scale (v,u) by $\bar{P}D_0^2/(\nu\rho L)$, where $\bar{P} = \rho\nu\omega\delta/\varepsilon^2$ is the scale for p. We further scale x by L, y by D_0, and time by $1/\omega$. Finally, we introduce the scaling $\xi_t = \delta D_0\omega\eta_t$, where $\eta(x,t)$ is dimensionless. Substituting all of this into the fluid equations, and retaining the original notation for the scaled variables, we obtain

$$\varepsilon^2 v_{xx} + v_{yy} = p_x + \alpha\varepsilon v_t, \tag{S5}$$

$$\varepsilon^2 u_{xx} + u_{yy} = \varepsilon^{-1}p_y + \alpha\varepsilon u_t, \tag{S6}$$

$$v_x + \varepsilon^{-1}u_y = 0. \tag{S7}$$

First order expansion. We expand $v = v^0 + \varepsilon v^1 + ...$ and similarly for p, u, and the flux $Q = \int_0^1 v(x,y)dy$. To leading order $p^0 = p^0(x,t)$, and $u^0 = u^0(x,t)$ due to [S6] and [S7]. However, the no-slip boundary conditions imply $u^0 = 0$. To leading order in δ the horizontal motion of the wall is negligible up to ε^3, and we retain only the vertical motion. Therefore, the kinematic boundary condition at $y = 0$ is

$$u(x, y = 0, t) = \varepsilon\eta_t. \tag{S8}$$

The leading order term v^0 satisfies $v^0_{yy} = p^0_x$ with boundary conditions $v^0(x,0,t) = v^0(x,1,t) = 0$. Therefore,

$$v^0(x,y,t) = \frac{p^0_x}{2}(y^2 - y), \quad Q^0 = -\frac{p^0_x}{12}. \tag{S9}$$

Integrating the incompressibility equation [S7] over $(0,1)$, and since to leading order $u = \varepsilon u^1$, we obtain

$$Q^0_x = -\int_0^1 u^1_y\, dy = \eta_t. \tag{S10}$$

Combining equations [S9] and [S10] provides an equation for the pressure $p^0_{xx} = -12\eta_t$. Given the boundary motion $\eta(x,t)$, this equation, together with boundary conditions for p^0, can be solved to find the pressure and from it the velocity v^0 and the flux Q^0.

Second order expansion. Since $u^0 = 0$, it follows from equation [S6] that also p^1 satisfies $p^1 = p^1(x,t)$. At the next order we obtain

$$v^1_{yy} = p^1_x(x,t) + \alpha v^0_t(x,y,t), \quad v^1(x,0,t) = v^1(x,1,t) = 0. \tag{S11}$$

Using equation [S9], v^0 can be expressed in the alternative form $v^0(x,y,t) = -6Q^0(x,t)(y^2 - y)$. Solving equation [S11] for v^1 we find

$$v^1 = \frac{p^1_x}{2}(y^2 - y) - \alpha\frac{Q^0_t}{2}(y^4 - 2y^3 + y).$$

Integrating v^1 over $(0,1)$ we obtain

$$Q^1 = -p^1_x/12 - \alpha Q^0_t/10\,. \tag{S12}$$

Addition of [S9] and [S12] gives the following equation, that is exact up to $O(\varepsilon)$:

$$Q + \zeta\frac{Q_t}{10} = -\frac{p_x}{12}, \tag{S13}$$

which is equivalent to equation [6].

bioRxiv preprint doi: https://doi.org/10.1101/760835; this version posted September 8, 2019. The copyright holder for this preprint (which was not certified by peer review) is the author/funder, who has granted bioRxiv a license to display the preprint in perpetuity. It is made available under aCC-BY-NC-ND 4.0 International license.

Similarly, up to $O(\varepsilon)$, $v(x,y,t) = -6Q(x,t)(y^2-y) - \zeta Q_t(x,t)(5y^4 - 10y^3 + 6y^2 - y)/10$. We recall that $Q(x,t)$ is available from the solution of the system of differential equations in our code. Once $v(x,y,t)$ is known, u can be obtained from [S4] and the boundary conditions, and the full equations [S2] and [S3] can be checked for self consistency. We have found that while the expansion above was carried out for values of ζ smaller than 1, numerical evidence indicates that equation [S13] is valid for much larger values of ζ. For instance, we consider a representative problem with $\zeta \sim 5$. Expansion up to $O(\varepsilon)$ entirely drops v_{xx} when evaluating p_x in [S5]. Support for this approximation can be based on Fig. S1, where we see that v_{xx} is significantly smaller than p_x. Similarly, Fig. S2 shows that p is essentially independent of y.

Critical Oscillators

Let us deal with an oscillator in which the signal f can be expressed in terms of the response x in the form

$$f = A(\omega, \Delta)x + B|x|^2 x + o(|x|^3)\,, \qquad \text{[S14]}$$

such that $A(\omega_c, \Delta_c) = 0$. The meaning of the symbols in this section is not necessarily the same as in the article. Here $|f|$ will be the amplitude of the BM motion, $|x|$ will be the amplitude of the IHB (between x and f there may be a phase) ω will have the meaning of frequency of the IHB (that either equals ω_{BM} or the frequency of spontaneous oscillations in the absence of signal), and Δ has the meaning of control parameter. Let us write $\Omega = \omega - \omega_c$, $\delta = \Delta - \Delta_c$ and assume that B can be approximated as constant and A can be expanded as

$$A = B(\alpha e^{i\chi_1}\Omega + \beta e^{i\chi_2}\delta)\,, \qquad \text{[S15]}$$

with $\alpha, \beta > 0$ and $\chi_{1,2} \in \mathbb{R}$.

In the case that there is no signal, $\alpha e^{i\chi_1}\Omega + \beta e^{i\chi_2}\delta + |x|^2 = 0$. From the imaginary part we obtain

$$\Omega(\delta) = -\frac{\beta \sin\chi_2}{\alpha \sin\chi_1}\delta \qquad \text{[S16]}$$

and then, from the real part,

$$|x|^2 = -\frac{\beta \sin(\chi_1 - \chi_2)}{\sin\chi_1}\delta\,. \qquad \text{[S17]}$$

Equation [S17] indicates that non-vanishing spontaneous responses occur either for $\delta > 0$ or for $\delta < 0$, depending on whether the signs of $\sin(\chi_1 - \chi_2)$ and $\sin\chi_1$ are opposite or the same. In our case, spontaneous responses are found for $\delta > 0$.

Let us now consider forced oscillations, $f \neq 0$. From [S14] and [S15] we have

$$|f|^2/|x|^2 = |B|^2[\alpha^2\Omega^2 + \beta^2\delta^2 + 2\alpha\beta\cos(\chi_1 - \chi_2)\Omega\delta + 2(\alpha\cos\chi_1\,\Omega + \beta\cos\chi_2\,\delta)|x|^2 + |x|^4]\,. \qquad \text{[S18]}$$

In particular, for $\Delta = \Delta_c$,

$$|f|^2/|x|^2 = |B|^2[\alpha^2\Omega^2 + 2\alpha\cos\chi_1\,\Omega|x|^2 + |x|^4]\,. \qquad \text{[S19]}$$

For small values of $|f|$, $|\delta|$ and $|\Omega|$, and for appropriately fitted values of Δ_c, ω_c, $|B|$, α, β, χ_1 and χ_2, our results are in good agreement with Eqs. [S16], [S17] and [S19].

Phase difference between nonsinusoidal functions

We consider two real functions, $f_1(t)$ and $f_2(t)$, that have the same period $2\pi/\omega$. We define the 'phase' ϕ of f_2 with respect to f_1 by the value that maximizes the overlap between these functions when the time is advanced in f_1 by ϕ/ω, i.e., by the value that maximizes $\oint f_1(t + \phi/\omega)f_2(t)dt$.

Equivalently, if we write $f_i(t) = \sum_{n=0}^{\infty} a_{ni}\cos[n(\omega t + \phi_{ni})]$, we have to maximize $\sum_{n=1}^{\infty} a_{n1}a_{n2}\cos[n(\phi + \phi_{n1} - \phi_{n2})]$, implying $\sum_{n=1}^{\infty} a_{n1}a_{n2}n\sin[n(\phi + \phi_{n1} - \phi_{n2})] = 0$. We note a dc component in any of the functions has no influence on the phase. If $f_1(t)$ and $f_2(t)$ have the same shape, then $\phi_{n1} - \phi_{n2}$ is independent of n and $\phi = \phi_{12} - \phi_{11}$.

In the case of quasi-sinusoidal functions, such that $|a_{n1}a_{n2}/a_{11}a_{12}| < \epsilon \ll 1$ for $n > 1$, we look for a solution $\phi = \phi_{12} - \phi_{11} + O(\epsilon)$. We expand $\sin[n(\phi + \phi_{n1} - \phi_{n2})] = \sin[n(\phi_{12} - \phi_{11} + \phi_{n1} - \phi_{n2})] + n\cos[n(\phi_{12} - \phi_{11} + \phi_{n1} - \phi_{n2})](\phi - \phi_{12} + \phi_{11}) + O(\epsilon^2)$ and obtain

$$\phi = \phi_{12} - \phi_{11} - \frac{\sum_{n=2}^{\infty} a_{n1}a_{n2}n\sin[n(\phi_{12} - \phi_{11} + \phi_{n1} - \phi_{n2})]}{a_{11}a_{12} + \sum_{n=2}^{\infty} a_{n1}a_{n2}n^2\cos[n(\phi_{12} - \phi_{11} + \phi_{n1} - \phi_{n2})]} + O(\epsilon^2)\,. \qquad \text{[S20]}$$

In our article $f_1(t)$ is proportional to $\cos\omega t$, so that the phase depends solely on the first harmonic of $f_2(t)$ and becomes

$$\phi = \phi_{12} = \arctan2\left[\oint \sin\omega t f_2(t)dt, \oint \cos\omega t f_2(t)dt\right]\,. \qquad \text{[S21]}$$

We note that the phase is not additive, i.e., the phase of f_3 with respect to f_1 not necessarily equals the phase of f_2 with respect to f_1 plus the phase of f_3 with respect to f_2.

bioRxiv preprint doi: https://doi.org/10.1101/760835; this version posted September 8, 2019. The copyright holder for this preprint (which was not certified by peer review) is the author/funder, who has granted bioRxiv a license to display the preprint in perpetuity. It is made available under aCC-BY-NC-ND 4.0 International license.

Number of cycles during which the traveling wave is amplified/attenuated

We want to estimate the number of cycles $n_{\rm cy}$ experienced by a wave of frequency $\omega_{\rm BM}$ as it travels across the region $z_1 \leq z \leq z_0$, where z_0 is the position (distance from the oval window) of the layer we consider and z_1 is the position where the wave starts to be amplified or attenuated significantly.

The dispersion relation can be obtained from Eqs. (2.17) and (2.40) (neglects damping) in (1):

$$k \tanh(kh) = \frac{\omega_{\rm BM}^2}{a[1-\omega_{\rm BM}^2/\omega_0^2(z)]}\,, \qquad \text{[S22]}$$

where k is the wave number, h the height of the chamber above or below the partition, a is a constant and $\omega_0(z)$ is the resonant frequency at position z.

For $kh \ll 1$ and $\omega_{\rm BM} \ll \omega_0(z)$, [S22] becomes $k^2 h = \omega_{\rm BM}^2/a$, and therefore $a = V^2(0)/h$, where $V(0)$ is the speed of the traveling wave in the long wavelength limit. For $\omega_{\rm BM}$ close to $\omega_0(z)$, kh is significantly larger than 1 and [S22] becomes

$$k = \frac{h\omega_{\rm BM}^2\omega_0^2(z)}{V^2(0)[\omega_0^2(z)-\omega_{\rm BM}^2]}\,. \qquad \text{[S23]}$$

The number of cycles is $n_{\rm cy} = (2\pi)^{-1}\int_{z_1}^{z_0} k(z)dz$. Assuming that $dw_0/dz = -\lambda w_0$ with constant λ, and using [S23] we obtain

$$n_{\rm cy} = \frac{h\omega_{\rm BM}^2}{2\pi\lambda V^2(0)}\int_{\omega_0(z_0)}^{\omega_0(z_1)} \frac{\omega_0 d\omega_0}{\omega_0^2-\omega_{\rm BM}^2} = \frac{h\omega_{\rm BM}^2}{4\pi\lambda V^2(0)}\ln\frac{\omega_0(z_1)^2-\omega_{\rm BM}^2}{\omega_0(z_0)^2-\omega_{\rm BM}^2}\,. \qquad \text{[S24]}$$

Taking $h = 0.0005$m, $\omega_{\rm BM} = 2\pi \times 5$kHz, $\lambda = 150\text{m}^{-1}$ (2) and $V(0) = 15$m/s (3), we obtain $h\omega_{\rm BM}^2/4\pi\lambda V^2(0) \approx 1$.

bioRxiv preprint doi: https://doi.org/10.1101/760835; this version posted September 8, 2019. The copyright holder for this preprint (which was not certified by peer review) is the author/funder, who has granted bioRxiv a license to display the preprint in perpetuity. It is made available under aCC-BY-NC-ND 4.0 International license.

Core of Mathematica Code

For further details, you are welcomed to contact the authors.

Geometric parameters

```
L = 10;  (* length of RL *)
LH = 10; (* length of HC *)
LT = L + 0.5 LH^2/(L + LH); (* length of TM *)
x1 = 3;  (* center of 1st OHC *)
x2 = 7;  (* center of 2nd OHC *)
ell = 2; (* extension of OHC in radial direction *)
```

Dynamic parameters

```
m = 10;           (* mass at each end of an OHC *)
mH = 120;         (* mass of HC *)
IRL = 2.*^3;      (* moment of inertia of RL *)
KRL = 1.*^3;      (* torsional spring constant on RL *)
KCP = 1.*^2;      (* spring constant between RL and CP *)
betaCP = 3;       (* damping constant between RL and CP *)
KC = 50;          (* spring constant between ends of OHC *)
betaC = 43;       (* damping constant between ends of OHC *)
DEL = 0.25375;    (* maximum contraction *)
KD1 = 4.*^2;      (* spring constant between 1st DC and BM *)
KD2 = 4.*^2;      (* spring constant between 2nd DC and BM *)
beta1 = 3;        (* damping 1st DC *)
beta2 = 3;        (* damping 2nd DC *)
beta12 = 3;       (* friction between DC 1-2 *)
KB = 10;          (* spring constant outer bundles *)
H1 = 6.5*^-3;     (* extension unstable range OHB1 *)
H2 = 5.*^-3 ;     (* extension unstable range OHB2 *)
KIHC = 10;        (* torsional spring constant inner bundle *)
HIN = 5.*^-3;     (* extension soft range IHB *)
cs = 2;           (* inner sulcus resistance to compression *)
mu = 10;          (* drag coefficient IHB *)
amp = 3 10^-5;    (* input amplitude *)
wbm = 5.3294;     (* input angular frequency *)
noise = 2.*^-6;   (* representative value for 2k_B T/thickness *)
```

Variables

(not executable cell)
q: $Q(0,t)$; tet: θ; b1: b_1; b2: b_2; s1: s_1; s2: s_2; tin: θ_{in}; pin: p_{in}
wn1, wn2, wn3, wn4: noise frequencies
ph1, ph2, ph3, ph4: noise phases

Initial values

```
(* Letter "p" stands for time derivative and "0" for initial value *)
tet0 = RandomVariate[NormalDistribution[0, Sqrt[noise/KRL]]];
tetp0 =  RandomVariate[NormalDistribution[0, Sqrt[noise/IRL]]] ;
b10 =  RandomVariate[NormalDistribution[0, Sqrt[noise/KCP]]];
b1p0 =  RandomVariate[NormalDistribution[0, Sqrt[noise/m]]];
b20 =  RandomVariate[NormalDistribution[0, Sqrt[noise/KCP]]];
b2p0 =  RandomVariate[NormalDistribution[0, Sqrt[noise/m]]];
s10 =  RandomVariate[NormalDistribution[0, Sqrt[noise/KD1]]];
s1p0 =  RandomVariate[NormalDistribution[0, Sqrt[noise/m]]];
s20 =  RandomVariate[NormalDistribution[0, Sqrt[noise/KD1]]];
s2p0 =  RandomVariate[NormalDistribution[0, Sqrt[noise/m]]];
pin0 = RandomVariate[NormalDistribution[0, Sqrt[noise cs]]];
q0 = 0; tin0 = 0;
```

bioRxiv preprint doi: https://doi.org/10.1101/760835; this version posted September 8, 2019. The copyright holder for this preprint (which was not certified by peer review) is the author/funder, who has granted bioRxiv a license to display the preprint in perpetuity. It is made available under aCC-BY-NC-ND 4.0 International license.

Input

```
ybm = amp Cos[wbm t]; (* signal; case of steady amplitude *)
an = Sqrt[0.5 noise/(KD1 + KD2)];
wn10 = RandomReal[{0, 2 wbm}];
wn20 = RandomReal[{0, 2 wbm}];
wn30 = RandomReal[{0, 2 wbm}];
wn40 = RandomReal[{0, 2 wbm}];
ph10 = RandomReal[{0, 2 Pi}];
ph20 = RandomReal[{0, 2 Pi}];
ph30 = RandomReal[{0, 2 Pi}];
ph40 = RandomReal[{0, 2 Pi}];
yn1 = an Cos[wn1[t] t - ph1[t]];
yn2 = an Cos[wn2[t] t - ph2[t]];
yn3 = an Cos[wn3[t] t - ph3[t]];
yn4 = an Cos[wn4[t] t - ph4[t]];
ytot = ybm+yn1+yn2+yn3+yn4; (*  signal + noise *)
```

x-dependence, forces and torques

```
(* evaluation of this cell may take a few seconds *)
ylow = tet[t] x + Piecewise[{{b1[t] (1 + Cos[2 Pi (x - x1)/ell]), x1 - ell/2 < x < x1 + ell/2},
       {b2[t] (1 + Cos[2 Pi (x - x2)/ell]), x2 - ell/2 < x < x2 + ell/2},
       {-tet[t] (L + LH) (x - L)^2/LH^2, x > L}}, 0];
qx = Integrate[Evaluate[D[ylow, t]], {x, 0, xx}, Assumptions -> xx > 0] /. xx -> x; (* Q(x,t)-Q(0,t) *)
px = -12 Integrate[Evaluate[qx + D[qx, t]/10] + q[t] + q'[t]/10, {x, LT, xx},
      Assumptions -> xx < LT] /. xx -> x // Simplify; (* p(x,t) *)
p0 = px /. x -> 0;
torqueRL = -Integrate[px x, {x, 0, x1 - ell/2}] - Integrate[px x, {x, x1 + ell/2, x2 - ell/2}] -
    Integrate[px x, {x, x2 + ell/2, L}] // Simplify; (* torque, pressure on RL *)
FH = -mH (5 L + LH) tet''[t]/12 - Integrate[px x, {x, L, LT}]/LH // Simplify; (* force, HC on RL *)
Fp1 = -Integrate[px, {x, x1 - ell/2, x1 + ell/2}]; (* force, pressure on CP1 *)
Fp2 = -Integrate[px, {x, x2 - ell/2, x2 + ell/2}]; (* force, pressure on CP2 *)
F1 = KCP b1[t] + betaCP b1'[t]; (* force, CP1 on RL *)
F2 = KCP b2[t] + betaCP b2'[t]; (* force, CP2 on RL *)
bund = KB Piecewise[{{-h - H, h < -H}, {-h + H, h > H}}, (H/Pi) Sin[Pi h/H]]; (* auxiliary *)
FB1 = bund /. h -> tet[t] x1 + b1[t] /. H -> H1; (* force, bundle on CP1 *)
FB2 = bund /. h -> tet[t] x2 + b2[t] /. H -> H2; (* force, bundle on CP1 *)
FC1 = KC (tet[t] x1 + b1[t] - s1[t] + DEL Tanh[(tet[t] x1 + b1[t])/H1]) +
   betaC (tet'[t] x1 + b1'[t] - s1'[t]); (* force, OHC on CP1 *)
FC2 = KC (tet[t] x2 + b2[t] - s2[t] + DEL Tanh[(tet[t] x2 + b2[t])/H2]) +
   betaC (tet'[t] x2 + b2'[t] - s2'[t]); (* force, OHC on CP2 *)
tauIHC = -KIHC Piecewise[{{tin[t] + HIN, tin[t] < -1.5 HIN}, {tin[t] - HIN, tin[t] > 1.5 HIN}},
    4 tin[t]^3/(27 HIN^2)]; (* torque, IHC on IHB *)
```

Dynamic equations

```
eqRL = Simplify[IRL tet''[t] == -KRL tet[t] + F1 x1 + F2 x2 + FH L + torqueRL];
eqCP1 = Simplify[m (tet''[t] x1 + b1''[t]) == -F1 + FB1 - FC1 + Fp1];
eqCP2 = Simplify[m (tet''[t] x2 + b2''[t]) == -F2 + FB2 - FC2 + Fp2];
eqD1 = Simplify[m s1''[t] == FC1 + KD1 (ytot - s1[t]) - beta1 s1'[t] + beta12 (s2'[t] - s1'[t])];
eqD2 = Simplify[m s2''[t] == FC2 + KD2 (ytot - s2[t]) - beta2 s2'[t] - beta12 (s2'[t] - s1'[t])];
eqIS = pin'[t] == -cs q[t];
eqP = pin[t] - p0 == mu (q[t] + tin'[t]/2);
eqIHB = tauIHC == mu (q[t]/2 + tin'[t]/3);
```

Time integration

```
tend = 1000; (* desired follow up lapse of time *)
sol = NDSolve[{eqRL, eqCP1, eqCP2, eqD1, eqD2, eqIS, eqP, eqIHB,
   tet[0] == tet0, tet'[0] == tetp0, b1[0] == b10, b1'[0] == b1p0,
   b2[0] == b20, b2'[0] == b2p0, s1[0] == s10, s1'[0] == s1p0,
   s2[0] == s20, s2'[0] == s2p0, tin[0] == tin0, q[0] == q0,
```

bioRxiv preprint doi: https://doi.org/10.1101/760835; this version posted September 8, 2019. The copyright holder for this preprint (which was not certified by peer review) is the author/funder, who has granted bioRxiv a license to display the preprint in perpetuity. It is made available under aCC-BY-NC-ND 4.0 International license.

```
  pin[0] == pin0, wn1[0] == wn10, wn2[0] == wn20, wn3[0] == wn30,
  wn4[0] == wn40, ph1[0] == ph10, ph2[0] == ph20, ph3[0] == ph30,
  ph4[0] == ph40,
  WhenEvent[Mod[t, 0.7] == 0.0, {prev = wn1[t], wn1[t] -> RandomReal[{0, 2 wbm}],
  ph1[t] -> Mod[ph1[t] + (wn1[t] - prev) t, 2 Pi]}],
  WhenEvent[Mod[t, 0.9] == 0.07, {prev = wn2[t], wn2[t] -> RandomReal[{0, 2 wbm}],
  ph2[t] -> Mod[ph2[t] + (wn2[t] - prev) t, 2 Pi]}],
  WhenEvent[Mod[t, 1.1] == 0.0707, {prev = wn3[t], wn3[t] -> RandomReal[{0, 2 wbm}],
  ph3[t] -> Mod[ph3[t] + (wn3[t] - prev) t, 2 Pi]}],
  WhenEvent[Mod[t, 1.3] == 0.070707, {prev = wn4[t], wn4[t] -> RandomReal[{0, 2 wbm}],
  ph4[t] -> Mod[ph4[t] + (wn4[t] - prev) t, 2 Pi]}]},
  {tet, q, b1, b2, s1, s2, pin, tin, wn1, wn2, wn3, wn4, ph1, ph2, ph3, ph4}, {t, 0, tend},
 DiscreteVariables -> {wn1, wn2, wn3, wn4, ph1, ph2, ph3, ph4}] [[1]];(* output information *)
```

Re-initialization for extension of follow up time

```
tet0 = tet[tend] /. sol ; tetp0 = tet'[tend] /. sol;
b10 =  b1[tend] /. sol; b1p0 = b1'[tend] /. sol;
b20 =  b2[tend] /. sol; b2p0 = b2'[tend] /. sol;
s10 =  s1[tend] /. sol; s1p0 = s1'[tend] /. sol;
s20 =  s2[tend] /. sol; s2p0 = s2'[tend] /. sol;
tin0 = tin[tend] /. sol; pin0 = pin[tend] /. sol;
q0 = q[tend] /. sol;
```

Amplitude and phase

```
tinit = tend - 7; (* beginning of desired lapse of time *)
tfin = tend - 2.1 Pi/wbm; (* end of desired lapse of time *)
func = tin[t] /. sol; (* pick desired function *)
t1 = t /. FindMaximum[func, {t, tinit, tinit + 0.1/wbm}][[2]];
(* refine lapse of time to obtain integer number of periods *)
t2 = t /. FindMaximum[func, {t, tfin, tfin - 0.1/wbm}][[2]];
average = NIntegrate[func, {t, t1, t2}, Method -> "Oscillatory",
    MaxRecursion -> 20, PrecisionGoal -> 2]/(t2 - t1);
averagesq = NIntegrate[func^2, {t, t1, t2}, Method -> "Oscillatory",
    MaxRecursion -> 20]/(t2 - t1);
amplitudesq = averagesq - average^2; (* this is the square of the amplitude *)
phase=ArcTan[NIntegrate[func Cos[wbm t], {t, t1, t2}],
   -NIntegrate[func Sin[wbm t], {t, t1, t2}]]; (* phase of func *)
```

bioRxiv preprint doi: https://doi.org/10.1101/760835; this version posted September 8, 2019. The copyright holder for this preprint (which was not certified by peer review) is the author/funder, who has granted bioRxiv a license to display the preprint in perpetuity. It is made available under aCC-BY-NC-ND 4.0 International license.

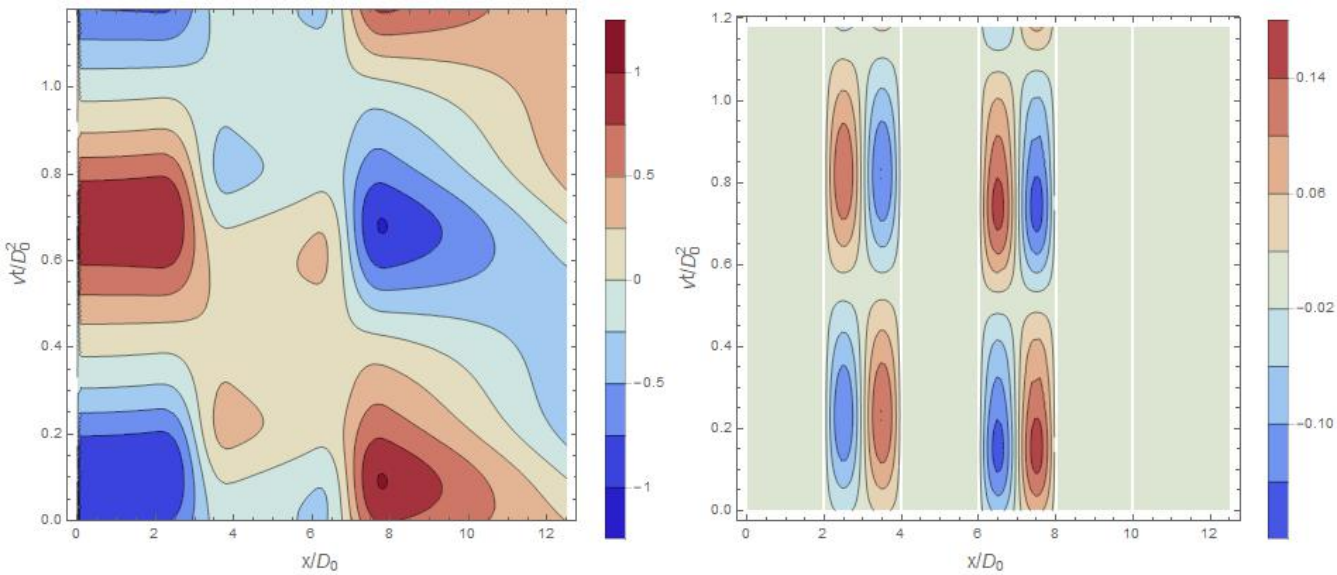

Fig. S1. Left: Contour plot of normalized pressure gradient, $(D_0^3/\rho\nu^2)\partial p/\partial x$, as a function of position and time, obtained using [S13] and thus neglecting $\varepsilon^2 v_{xx}$ in [S5]. Right: y-average of the neglected term,$(D_0^2\nu)\int_0^{D_0} dy\partial^2 v/\partial x^2$. The white lines are places where v_{xx} is discontinuous. The time span describes one cycle, beginning and ending when θ assumes its most negative value. For disambiguation, all quantities in the legends and in this caption are dimensional. The color scale bars are different for each graph.

bioRxiv preprint doi: https://doi.org/10.1101/760835; this version posted September 8, 2019. The copyright holder for this preprint (which was not certified by peer review) is the author/funder, who has granted bioRxiv a license to display the preprint in perpetuity. It is made available under aCC-BY-NC-ND 4.0 International license.

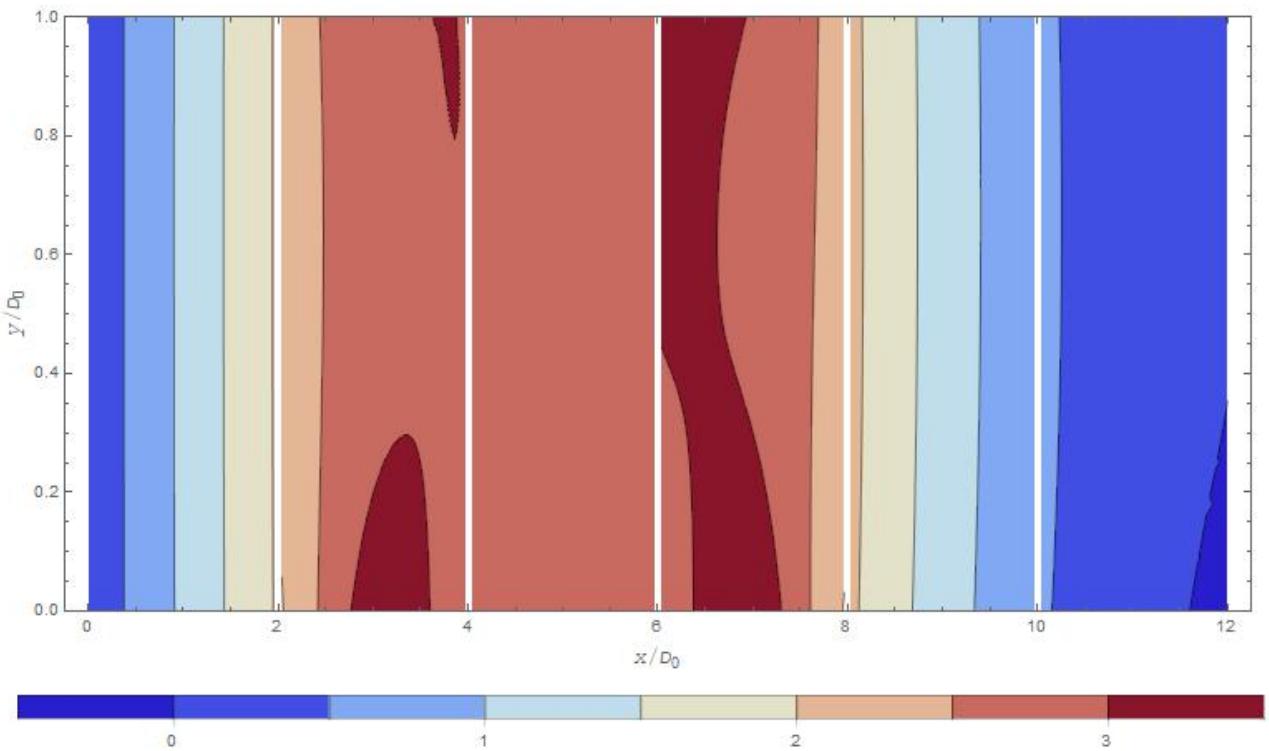

Fig. S2. Pressure $p(x, y, t = 1.2\pi/\omega_{\mathrm{BM}})$ in the in the subtectorial channel. The pressure unit in the color scale bar is $\rho\nu^2/D_0^2$. At the moment depicted in this snapshot the RL is moving downwards and the CPs are moving upwards. At the white lines the pressure is discontinuous, but since the y-dependence is small the discontinuity is not visible in the figure. For $t \neq 1.2\pi/\omega_{\mathrm{BM}}$, $|p(x, y = 0.5D_0, t) - p(x, y = 0, t)|$ is typically smaller.

bioRxiv preprint doi: https://doi.org/10.1101/760835; this version posted September 8, 2019. The copyright holder for this preprint (which was not certified by peer review) is the author/funder, who has granted bioRxiv a license to display the preprint in perpetuity. It is made available under aCC-BY-NC-ND 4.0 International license.

References

1. Reichenbach T, Hudspeth AJ (2014) The physics of hearing: fluid mechanics and the active process of the inner ear. *Rep Prog Phys* **77** 076601
2. Greenwood DD (1990) A cochlear frequency-position function for several species-29 years later. *J Acoust Soc Amer* **87** 2592–2605
3. Lighthill J (1981) Energy flow in the cochlea. *J Fluid Mech* **106** 149–213